7.2. Glacially Induced Faulting in Alaska

Jeanne Sauber, Chris Rollins, Jeffrey T. Freymueller, Natalia A. Ruppert

Abstract

Southern Alaska provides an ideal setting to assess how surface mass changes can influence crustal deformation and seismicity amidst rapid tectonic deformation. Since the end of the Little Ice Age, the glaciers of southern Alaska have undergone extensive wastage, retreating by kilometers and thinning by hundreds of meters. Superimposed on this are seasonal mass fluctuations due to snow accumulation and rainfall of up to meters of equivalent water height in fall and winter, followed by melting of gigatons of snow and ice in spring and summer and changes in permafrost. These processes produce stress changes in the solid Earth that modulate seismicity and promote failure on upper-crustal faults. Here we quantify and review these effects and how they combine with tectonic loading to influence faulting in the southeast, St. Elias and southwest regions of mainland Alaska.

7.2.1. Introduction and Tectonic Setting

In southern Alaska, a strong seasonal cycle of snow accumulation and melt is superimposed on a high rate of interannual glacier mass wastage. The magnitudes of both are spatially and temporally variable, as seen in Gravity Recovery and Climate Experiment (GRACE)-derived observations across the region (**Fig. 7.2.1**). These mass changes occur directly atop the southern Alaska plate boundary zone, which transitions from mainly strike-slip faulting in southeast Alaska to mainly upper-crustal thrusting in the St. Elias region to subduction along the Alaska-Aleutian megathrust further west.

Figure. 7.2.1 a. *Overview of study region and locations of major glaciers. BIV: Bagley Ice Valley, BG: Bering Glacier, GB: Glacier Bay, HIF: Harding Icefield, IB: Icy Bay, MG: Malaspina Glacier, US: Upper Seward Glacier, location of 2014 M=6 oblique-slip earthquake. Background image: Moderate Resolution Imaging Spectroradiometer (MODIS) image from August 9, 2003. Colored stars: locations of mass changes plotted in b.* ***b.*** *Recent cryospheric changes in cm water equivalent (w.e.) estimated from Gravity Recovery and Climate Experiment (GRACE)-derived mass change (mascons) for the Southeastern, St. Elias, and Southwest regions of coastal Alaska. The 2003-2016 data used are available at https://neptune.gsfc.nasa.gov/gngphys/index.php?section=470 (Luthcke et al., 2013; Loomis & Luthcke, 2014).*

Southeast Alaska features the largest average seasonal signal of the three regions (~40 cm water equivalent, w.e.), superimposed on ongoing ice wastage with an interannual trend of approximately 14 cm/yr w.e. (2003-2016) (**Fig. 7.2.1**). This coastal region has been undergoing rapid post-Little Ice Age (LIA) deglaciation since ~1770, particularly in the Glacier Bay region, which alone has lost >3000 km^3 of ice (Larsen *et al.,* 2005). At present, the solid-Earth isostatic response to past and ongoing mass loss

produces surface uplift rates of up to >3 cm/yr (among the fastest on Earth) and >7 mm/yr of horizontal motion centered on Glacier Bay (Larsen *et al.,* 2005; Hu & Freymueller, 2019). Running beneath and alongside this rapid deformation is the strike-slip Fairweather Fault, which is the effective plate boundary in southeast Alaska, accommodating >4 cm/yr of right-lateral motion (Fletcher & Freymueller, 2003; Elliott *et al.,* 2010; Koehler & Carver, 2018). The Fairweather Fault has ruptured in four M≥7 earthquakes since 1927 (Doser & Lomas, 2000) including a M=7.8 earthquake in 1958 that nucleated southwest of Glacier Bay (Plafker *et al.,* 1978; Doser, 2010) (**Fig. 7.2.2**). The northwest Fairweather Fault connects to the St. Elias compressional margin, the site of two M~8.1 thrust earthquakes in 1899 (Plafker & Thatcher, 2008) and a M_s=7.4 event in 1979. Here we evaluated how post-1770 ice loss may have influenced these and other recent earthquakes.

The St. Elias margin has the most rapid present-day ice wastage of the three regions (17 cm/yr w.e.) as well as an average seasonal load amplitude of ~35 cm w.e. (**Fig. 7.2.1**). Post-LIA deglaciation in this region began around 1880 between the Malaspina and Bering Glaciers and likely induces up to 10-20 mm/yr of viscoelastic uplift at present day (Sauber *et al.*, 1997; 2000; Elliott *et al.* 2013). The St. Elias region is undergoing rapid NNW-SSE tectonic compression and uplift as the Pacific plate carries the thick Yakutat block into and beneath interior Alaska (*Sauber et al.,* 1997; Chapman *et al.,* 2008; Bruhn *et al.,* 2012; Elliott *et al.,* 2013). Here we reviewed and evaluated the influence of seasonal and interdecadal mass changes on the thrust and oblique-slip faulting that pervades this area.

The eastern Alaska-Aleutian subduction zone features more modest interannual (~9 cm/yr w.e.) and seasonal (22 cm w.e.) cryospheric changes (**Fig. 7.2.1,** Southwest), but also ruptures in great earthquakes including the 1964 M=9.2 Alaska earthquake, as well as multiannual slow-slip events (e.g., Li & Freymueller, 2018). Here we explored the influence of mass changes on the initiation of slow-slip events beneath the Harding Icefield on the Kenai Peninsula.

7.2.2. Cryosphere-Solid Earth Interactions and Large Earthquakes in Southeast Alaska

To estimate the history of cryosphere-related stress changes in southeast Alaska (**Fig. 7.2.2b**), we used the model of Hu and Freymueller (2019 and references therein), which couples an ice history model with an elastic-viscoelastic Earth structure. The Earth model comprises a 55-km-thick elastic layer overlying a 230-km-thick linear viscoelastic asthenosphere with Maxwell viscosity $3 \cdot 10^{19}$ Pa · s. In a three-dimensional search over lithosphere thickness, asthenosphere thickness and viscosity, Hu and Freymueller (2019) found that this combination of the three parameters (coupled with the ice model) produced the best fit to interannual uplift rates extracted from 20 years of GPS data in the region. Their original model and parameter search used TABOO (Spada *et al.,* 2003), which does not calculate stress, so we converted the model to Relax (Barbot & Fialko, 2010a,b) to calculate stress changes on faults. To

compute stress changes on faults in a way that accounts for the change in dominant faulting type between Southeast Alaska and the St. Elias, we computed the full history of the stress change tensor at 10 km depth, then calculated the changes in Coulomb failure stress (see discussion in Steffen *et al.,* 2021, Chapter 2) on a grid of variable receiver fault plane orientations and slip directions spatially interpolated from those of major faults in the Alaska Division of Geological and Geophysical Survey's Quaternary Faults and Folds map, augmented with the block boundaries in the Elliott *et al.* (2013) St. Elias block model.

Figure 7.2.2 a. *Post-1770 ice loss, related stress changes and recent earthquakes in southeast Alaska. Grayscale squares: regions of ≥50 m total 1770-1958 ice loss in the model of Hu and Freymueller (2019, see references within for specifics of ice loss history), colored and annotated (italics) by total ice loss. Areas of <50 m total ice loss are omitted for readability. Colored surface: total 1770-1958 Coulomb stress changes imparted to faults in Southeast Alaska by the integrated elastic and viscoelastic responses to the ice loss, as computed with the Hu and Freymueller (2019) ice and Earth structure model. The full stress change tensor field was computed at 10 km depth, then Coulomb stress changes were calculated by projecting onto a grid of variable receiver fault plane orientations and slip directions spatially interpolated from those of major faults (black lines), capturing the spatial variation in faulting type. We assumed an effective friction of 0.4. Beach balls: focal mechanisms of earthquakes since 1899 (Doser & Lomas, 2000; Johnson et al., 2020).* ***b.*** *Location of study region.* ***c-f.*** *For physical intuition, we use a reference model of a 100-km-wide ice mass losing 1 m/yr of equivalent water height alongside a vertical right-lateral strike-slip fault, within the same Hu and Freymueller (2019) Earth structure.* ***c****. Model setup.* ***d****. Cumulative shear stress changes for right-lateral slip after 200 yr of melting and viscoelastic rebound (MPa). (Colors would be reversed for a left-lateral strike-slip fault.)* ***e****. Normal stress changes (MPa), positive for unclamping (reduction in normal stress).* ***f.*** *Coulomb stress changes (MPa) assuming an effective friction of 0.4.*

Our main finding is that pre-1958 ice loss and viscoelastic rebound loaded the future epicenter of the 1958 M=7.8 Fairweather Fault earthquake with a 0.2-0.3-MPa (2-3-bar) increase in Coulomb stress (**Fig. 7.2.2a**). These stress changes can be understood physically via a simple reference model of a vertical strike-slip fault with a thinning surface load abutting the left side of the fault in the fault's strike direction (**Fig. 7.2.2c-f**), within the same Hu and Freymueller (2019) Earth structure. This reference model shows that cryosphere-induced deformation increases the shear stress for right-lateral slip ahead of the load in the strike direction (**Fig. 7.2.2d**) (the opposite for left-lateral slip) and unclamps (reduces the confining stress on) the fault alongside the thinning load (**Fig. 7.2.2e**), summing to a Coulomb stress increase for right-lateral slip (promoting fault instability) whose maximum is near the corner of the load (**Fig. 7.2.2f**). In southeast Alaska, the location of the Glacier Bay unloading was such that the 1958

epicenter was located near this maximum, on the only section of the right-lateral Fairweather Fault on which both the shear and normal stress were increased (**Fig. 7.2.2a**). Although a 0.2-0.3-MPa stress change is equivalent to just ~2-3 years of tectonic loading on the fast-slipping Fairweather Fault, these results suggest that cryosphere-solid Earth interactions may have affected the nucleation and characteristics of the 1958 earthquake (Rollins *et al.*, in prep, 2020).

Like the earlier calculations given in Sauber *et al*. (2000), Sauber and Molnia (2004) and Sauber and Ruppert (2008), our results using the Hu and Freymueller (2019) model in the St. Elias indicate that ice loss and viscoelastic rebound increased the Coulomb stress on thrust faults there, likely promoting the 1979 (M_s=7.4) St. Elias earthquake and/or its rich aftershock sequence (**Fig. 7.2.2a**). In fact, nearly all known M≥6 20th-century earthquakes in southeast Alaska (Doser & Lomas, 2000; Johnson *et al.,* 2020) appear to have occurred at locations where the post-LIA cryosphere-solid Earth interactions would have increased rather than decreased Coulomb stress on faults (**Fig. 7.2.2a**). This correlation should not be oversold as all of these earthquakes also occurred within the rapidly deforming plate boundary zone; nevertheless, it suggests that stress changes from cryosphere-solid Earth interactions are worth considering in regional seismic hazard models.

7.2.3. Ice Mass Fluctuations and Earthquakes in the St. Elias Region

Our previous work in the St. Elias region comprised two main approaches. In the first, we estimated the possible stress influence of post-LIA ice loss on the 1979 St. Elias earthquake (Sauber *et al.,* 2000; Sauber & Ruppert*,* 2008, and refs. therein). We used a two-dimensional finite element model with a simple geology-based representation of ice loss to calculate the incremental stresses and change in fault stability along the shallow dipping main thrust zone (MTZ) and at the surface. Along the MTZ, our results indicated that the region between the coast and the 1979 aftershock zone had been brought closer to failure by 0.2–1.2 MPa by 1979. In the second approach, we used the strong seasonal variations and the modern-day seismic catalog to vet the hypothesis that these Coulomb stress changes can influence earthquake behavior. We found that background seismicity rates vary seasonally and also appeared to vary interannually in a seasonally dependent way (between 1988-2006.9), with stronger seasonal fluctuations in warmer-than-average years than in colder years.

Recently, we extended this analysis by (1) calculating the *annual* 3D stresses and Coulomb stress changes associated with tectonic loading to place the stresses from cryospheric fluctuations in context, (2) improving the estimate of cryosphere-related stress changes by incorporating GRACE and other decadal-scale mass change data, (3) using updated and relocated seismicity data to evaluate the modulation of seismic energy release and testing for a cryospheric influence on hypocenter depth, and (4) using well-constrained focal mechanisms to estimate stress orientations as a function of time.

To calculate the first-order features of annual tectonic stresses and surface displacements, we used a 3-D finite element model (FEM) of a subduction zone in PyLith (Aagaard *et al.,* 2017). Our model consisted of a slab and a subduction interface of which the shallow portion (<40 km) was locked and the deeper portion creeps at the rate of Pacific-North American plate convergence (5 cm/yr). Our results indicate up to 4 cm/yr of ~N-S horizontal contraction onshore and tectonic uplift rates that range from <1 mm/yr to 1 cm/yr further inland. The corresponding annual tectonic stressing rate has a maximum principal stress (σ_1, directed ~North) of up to 20 kPa/yr, whereas the vertical stress rate (σ_V) is <4 kPa/yr. These stress changes increased promoted Coulomb failure on faults by ~9 kPa/year.

Figure 7.2.3 *St. Elias region: Schematic diagram of calculated seasonal surface displacements (left) and changes in Coulomb stress for WY05 assuming an optimal, pre-existing fault orientation (see Steffen et al., 2021, Chapter 2) for regions close to the coast and ~50 km inland in the Bagley Ice Valley (BIV in* ***Fig. 7.2.1****). Top: modeled loading in the late fall to early spring induces mm of horizontal displacement (black arrows, left) and ~cm of subsidence, promoting fault stability (top right). Bottom: The same but for the surface unloading scenario during the spring to early fall that leads to fault instability. *This calculation assumes most of the winter snow melts in the summer, so it represents an upper bound for the displacements and fault stability changes.*

To compare with the stresses associated with cryospheric changes, we used PyLith to estimate the incremental crustal displacements and stresses due to seasonal mass variations and annual wastage during Water Year 2005 (2004.8 – 2005.8; this year represents an average year with net mass loss). We used a layered rheological model with a 40-km (effective) elastic layer over a viscoelastic layer (Sauber *et al.,* 2016). The magnitude and timing of the fluctuations were estimated using GRACE 1° x 1° degree mascon results (**Fig. 7.2.1**) validated qualitatively with GPS reflectometry (K. Larson, cGPS site, AB09), glacier studies (Muskett *et al.,* 2008a,b, 2009), and snow depth change as a function of elevation estimated from another mountainous region (Kirchner *et al.,* 2014). **Figure 7.2.3** shows how incremental stresses and Coulomb stress changes vary between fall/winter and spring/summer and between the Gulf of Alaska coast and the Bagley Ice Valley ~80 km inland (BIV, **Fig. 7.2.1**). In winter the more abundant snow north of the coast at higher altitudes causes subsidence and tilting toward the north (near coast), moving the faults away from failure on the thrust faults that pervade this environment. In contrast, from late March until the early fall, the melting of this snow and ice produces uplift and tilting toward the south in the coastal region, promoting Coulomb failure there by 5 kPa. However, the maximum Coulomb stress increase is inland in the Bagley Ice Valley (26 kPa) due to both uplift and north-directed horizontal motions that are similar in orientation to those from tectonic loading. At GPS site AB35, along the coast between Icy Bay and the Bering Glacier, we observed seasonal oscillations in the

detrended position time series comparable to those predicted by these calculations (Fu *et al.,* 2012; Sauber *et al.,* 2016).

Figure 7.2.4 *Total energy released by tectonic events per month over four different time periods. Energy of an earthquake is defined as LogE=11.8+1.5*M. Earthquake data is from the Alaska Earthquake Center catalog supplemented with the STEEP dataset (Bruhn et al., 2012). Icy Bay region is defined as 140.4-142.2W and 59.7-60.5N. Only tectonic earthquakes were included (9,135 within the Icy Bay region). Note the increase of seismic energy release in fall during all time periods.*

To best evaluate the influence of seasonal cryospheric change on seismicity, we estimated temporal variations in the seismic energy release per month and examined relocated hypocentral depths for the Icy Bay region given in Sauber and Ruppert (2008). We examined seasonal fluctuations in seismic energy release rates (**Fig. 7.2.4**) over four time periods: (1) July 2005- June 2010, which featured the lowest detection threshold thanks to the additional coverage provided by the STEEP project (Bruhn *et al.,* 2012), providing the best baseline for background seismicity); (2) Nov. 2009 – Oct. 2012, (3) Nov. 2012 – Oct. 2015, and (4) Nov. 2015 – Sept. 2018. Seismic energy release rates notably increased in late fall in all time periods. Although our earlier study suggested that this seasonality may be stronger during warmer-than-average years, here all time periods showed a similar seasonal dependence. In parallel, tests for seasonal variability in the hypocentral depths of relocated earthquakes with M≥1.4 (the overall magnitude of completeness over the 2005-2018 period) revealed no systematic depth variations between seasons or between the four time periods. The largest earthquake in the St. Elias region between 2005 and 2018 was a M_w=6.0 event below the Upper Seward Glacier (**Fig. 7.2.1**) on 17 July 2014. This shallow event (6 km depth) occurred at the end of the high-altitude melt season during a period of maximum fault instability (**Fig. 7.2.3).**

Although the predicted seasonal stresses are small relative to total stress levels (Sauber *et al.,* 2000 and references therein), we tested whether well-constrained stress tensors from the study region changed between the summer and winter months, especially in the vertical component (σ_V). We used P-wave first motion focal mechanisms to compute best-fitting stress tensors in the Icy Bay region following the approach given in Ruppert (2008). We divided the dataset into 4-month-long seasons (summer and winter periods) and compared them to the stress tensor orientations from the full year (**Fig. 7.2.5**). The resulting stress tensors for the total dataset versus summer or winter were within statistical uncertainties of each other; however, there is a hint that the vertical component (σ_3) migrates to be more vertical in summer than the year-round average.

.

Figure 7.2.5 *Best-fitting stress tensors for events in the Icy Bay area for all months (left), May-August only (middle) and November-February only (right). Open squares, triangles and circles represent best-fitting maximum, intermediate and minimum stress directions, respectively; parameters given at the bottom of plots. Shaded areas show uncertainty levels as computed by a bootstrapping technique.*

7.2.4. Evaluating the Influence of Seasonal Fluctuations on Slow-Slip below the Harding Icefield

Although the seasonal and interannual mass changes in the eastern Alaska-Aleutian subduction zone (**Fig. 7.2.1**), are milder than in the other two regions, we explored their influence on the onset of slow-slip events (effectively very slow earthquakes, similarly involving fault slip). In Cook Inlet, slow slip events occur on the interface between the subducting Pacific plate and the overriding plate and tend to last several years (e.g., Li & Freymueller, 2018). They occur at depths of ~30-50 km, deeper than large 1964-style thrust earthquakes and near the transition from unstable (stick-slip) to stable friction. Lowry (2006) found a periodicity in slow-slip events in Guerrero, Mexico, and proposed that they may occur in response to climate-driven stress perturbations. Although the lower Cook Inlet slip events do not show an obvious periodicity, they do tend to begin in the late fall/early winter, similar to the peak in seismicity rate.

Here we compared documented slow-slip events (Li & Freymueller, 2018) to the predicted changes in Coulomb stress in the region of slow slip events. To calculate the seasonal stress changes prior to one of the slow-slip events (2010.8-2011), we ran a PyLith model with seasonal snow loading and unloading plus interannual ice wastage on the Harding Icefield. The location of maximum predicted fault stability change roughly corresponds to the upper portion of the 2004 slow-slip event (~35 km depth). We calculated that snow accumulation between Nov. 2009 and March 2010 promoted fault stability there by 1.2 kPa while melting and ongoing wastage in the summer months preceding the event (April – early October 2010) produced uplift and tilting in the approximate direction of plate convergence, promoting fault instability by 1.3 kPa. These minor changes may have had a small influence on promoting in time the initiation of the 2010.8 slow-slip event.

7.2.5. Summary and Future Work

In this study we summarized previous and new work evaluating the influence of cryospheric fluctuations on fault slip in three tectonically distinct regions of southern Alaska: the strike-slip plate boundary in the southeast, the St. Elias crustal collision zone, and the eastern Alaska-Aleutian subduction zone. In the southeast, long-term ice wastage may promote major earthquakes in time, though it represents a second-order perturbation on top of the rapid tectonic loading. For the dominantly thrust-faulting environment of the St. Elias, and to a less extent slow-slip events below the Harding Icefield region,

seasonal unloading can lead to significant changes in the fault stability relative to annual tectonic loading rates, but these changes are quite localized.

As noted in Hardebeck (2004) and Parsons (2005), a sudden change in stress due to an earthquake or rapid cryospheric change (seasonal ablation or a glacial surge) is only likely to change earthquake probabilities over a time interval that is short compared to the repeat time of large earthquakes (Sauber *et al.,* 1995; Sauber *et al.,* 2000; Sauber & Ruppert, 2008). These localized, transient stresses might thus have a more testable effect on small and moderate earthquakes. An additional complexity was highlighted by Johnson *et al*. (2019), who conducted a systematic study of shallow, M>2.0 earthquakes across southern Alaska to test for seasonal variations during the annual hydrological cycle. Their results indicated a general increase in regional seismicity rates in the late fall that lags behind the optimal conditions for promoted fault slip by ~3 months, similar to their findings in some regions of California (Johnson *et al.,* 2017). To date, the effect of recent regional, time-dependent stresses due to glacial wastage on faulting potential has not been evaluated in any Alaska-wide earthquake hazard assessment (Mueller *et al.,* 2015).

Acknowledgements

We thank Holger Steffen and two anonymous reviewers for their constructive reviews of our submission and Rebekka Steffen for providing Chapter 2 in advance of publication. Funding for this study for J. Sauber, J. Freymueller and C. Rollins was provided by NASA's Earth Surface and Interior grant 15-ESI2015-0051 and GRACE-FO science team grant 15-GRACE15-0006 (J. Sauber). This research was supported in part by the Geophysical Institute, University of Alaska Fairbanks (N. A. Ruppert).

References

Aagaard, B., Knepley, M., and Williams, C. (2017). PyLith v2.2.1, Computational Infrastructure for Geodynamics, DOI: https://doi.org/10.5281/zenodo.886600, url: https://geodynamics.org/cig/software/pylith/

Barbot, S., and Fialko, Y. (2010a). Fourier-domain Green's function for an elastic semi-infinite solid under gravity, with applications to earthquake and volcano deformation. *Geophysical Journal International,* **182**(2), 568–582, DOI: https://doi.org/10.1111/j.1365-246X.2010.04655.x.

Barbot, S., and Fialko, Y. (2010b). A unified continuum representation of postseismic relaxation mechanisms: Semi-analytic models of afterslip, poroelastic rebound and viscoelastic flow. *Geophysical Journal International,* **182**(3), 1124–1140. DOI: https://doi.org/10.1111/j.1365-246X.2010.04678.x.

Bruhn, R.L., Sauber, J., Cotton, M.M., Pavlis, T.L., Burgess, E., Ruppert, N., and Forster, R.R. (2012). Plate margin deformation and active tectonics along the northern edge of the Yakutat Terrane in the Saint Elias Orogen, Alaska, and Yukon, Canada. *Geosphere,* **8**(6)*,* 1384–1407, DOI: https://doi.org/10.1130/GES00807.1.

Chapman, J.B., *et al. (*2008). Neotectonics of the Yakutat Collision: Changes in Deformation Driven by Mass Redistribution. American Geophysical Union: Active Tectonics and Seismic Potential of Alaska. *Geophysical Monograph Series 179*. DOI: https://doi.org/10.1029/179GM21.

Doser, D. (2010). A Re-evaluation of the 1958 Fairweather, Alaska, Earthquake Sequence. *Bulletin of the Seismological Society of America*, **100**(4), 1792-1799. DOI: https://doi.org/10.1785/0120090343.

Doser, D. I., and Lomas, R. (2000). The transition from strike-slip to oblique subduction in southeastern Alaska from seismological studies. *Tectonophysics,* **316**, 45–65, DOI: https://doi.org/10.1016/S0040-1951(99)00254-1.

Elliott, J., Larsen, C.F., Freymueller, J.T., and Motyka, R.J. (2010). Tectonic block motion and glacial isostatic adjustment in southeast Alaska and adjacent Canada constrained by GPS measurements. *Journal of Geophysical Research,* **115**, B09407. DOI: https://doi.org/10.1029/2009JB007139.

Elliott, J., Freymueller, J.T., and Larsen, C.F. (2013). Active tectonics of the St. Elias orogen, Alaska, observed with GPS measurements. *Journal of Geophysical Research Solid Earth*, **118**, 5625–5642. DOI: https://doi.org/10.1002/jgrb.50341.

Fletcher, H. J., and Freymueller, J.T. (2003), New constraints on the motion of the Fairweather Fault, Alaska, from GPS observations. *Geophysical Research Letters,* **30**(3), 1139. DOI: https://doi.org/10.1029/2002GL016476.

Fu, Y., Freymueller, J.T., and Jensen, T. (2012). Seasonal hydrological loading in southern Alaska observed by GPS and GRACE. *Geophysical Research Letters,* **39**(15)*,* DOI: https://doi.org/10.1029/2012GL052453.

Hardebeck, J. L. (2004). Stress triggering and earthquake probability estimates. *Journal of Geophysical Research,* **109**, B04310, DOI: https://doi.org/ 10.1029/2003JB002437.

Hu, Y., and Freymueller, J.T. (2019). Geodetic observations of time-variable glacial isostatic adjustment in southeast Alaska and its implications for Earth rheology. *Journal of Geophysical Research,* **124**(9), 9870–9889, DOI: https://doi.org/10.1029/2018JB017028.

Johnson, C.W., Fu, Y., and Bürgmann, R. (2017). Stress models of the annual hydrospheric, atmospheric, thermal, and tidal loading cycles on California faults: Perturbation of background stress and changes in seismicity. *Journal of Geophysical Research: Solid Earth,* **122**(12), 10,605–10,625, DOI: https://doi.org/10.1002/2017JB014778.

Johnson, C. W., Fu, Y., and Bürgmann, R. (2020). Hydrospheric modulation of stress and seismicity on shallow faults in southern Alaska. *Earth and Planetary Science Letters,* **530**, 115904 DOI: https://doi.org/10.1016/j.epsl.2019.115904.

Kirchner, P.B., Bales, R.C., Molotch,N.P, Flanagan, J., and Guo, Q. (2014). LiDAR measurement of seasonal snow accumulation along an elevation gradient in the southern Sierra Nevada, California. *Hydrology and Earth System Sciences,* **18**(10), 4261–4275, DOI: https://doi.org/10.5194/hess-18-4261-2014.

Koehler, R.D., and Carver, G.A. (2018). Active Faulting and Seismic Hazards in Alaska. Alaska Division of Geological and Geophysical Surveys, Miscellaneous Publication 160.

Larsen, C.F., Motyka, R.J., Freymueller, J.T., Echelmeyer, K.A., and Ivins, E.R. (2005). Rapid viscoelastic uplift in southeast Alaska caused by post-Little Ice Age glacial retreat. *Earth and Planetary Science Letters,* **237**(3-4), 548–560, DOI: https://doi.org/10.1016/j.epsl.2005.06.032.

Li, S., and Freymueller, J.T. (2018). Spatial variation of slip behavior beneath the Alaska Peninsula along Alaska-Aleutian subduction zone. *Geophysical Research Letters,* **45**(8), 3453–3460, https://doi.org/10.1002/2017GL076761.

Loomis, B.D., and Luthcke, S.B. (2014). Optimized signal denoising and adaptive estimation of seasonal timing and mass balance from simulated GRACE-like regional mass variations. *Advances in Adaptive Data Analysis,* **6**(1), 1450003, DOI: https://doi.org/10.1142/S1793536914500034.

Lowry, A.R. (2005). Resonant slow fault slip in subduction zones forced by climatic load stress. *Nature,* **442**, DOI: https://doi.org/10.1038.

Luthcke, S.B., Sabaka, T.J., Loomis, B.D., Arendt, A.A., McCarthy, J.J., and Camp, J. (2013). Antarctica, Greenland and Gulf of Alaska land-ice evolution from an iterated GRACE global mascon solution. *Journal of Glaciology*, **59**(216), 613–631, DOI: https://doi.org/10.3189/2013JoG12J147.

Mueller, C.S., Briggs, R.W., Wesson, R.L., and Petersen, M.D. (2015). Updating the USGS seismic hazard maps for Alaska. *Quaternary Science Reviews*, **113**, 39–47, DOI: https://doi.org/10.1016/j.quascirev.2014.10.006.

Muskett, R.R., Lingle, C. S., Sauber, J.M., Rabus, B.T., and Tangborn, W. V. (2008a). Acceleration of surface lowering on the tidewater glaciers of Icy Bay, Alaska, USA from InSAR DEMs and ICESat altimetry. *Earth and Planetary Science Letters*, **265**(3-4), 345–359, DOI: https://doi.org/10.1016/j.epsl.2007.10.012.

Muskett, R.R., Lingle, C. S., Sauber, J. M., Post, A.S., Tangborn, W.V., and Rabus, B.T. (2008b). Surging, accelerating surface lowering and volume reduction of the Malaspina Glacier system, Alaska, USA, and Yukon, Canada, from 1972 to 2006. *Journal of Glaciology*, **54**(188), 788–800, DOI: https://doi.org/10.3189/002214308787779915.

Muskett, R.R., Lingle, C.S., Sauber, J.M., Post, A.S., Tangborn, W.V., Rabus, B.T., and. Echelmeyer, K. A. (2009). Airborne and spaceborne DEM-and laser altimetry-derived surface elevation and volume changes of the Bering Glacier system, Alaska, USA, and Yukon, Canada, 1972–2006. *Journal of Glaciology*, **55**(190), 316–326, DOI: https://doi.org/10.3189/002214309788608750.

Parsons, T. (2005). Significance of stress transfer in time-dependent earthquake probability calculations. *Journal of Geophysical Research,* **110**, B05S02, DOI: https://doi.org/10.1029/2004JB003190.

Plafker, G., and Thatcher, W. (2008). Geological and geophysical evaluation of the mechanisms of the great 1899 Yakutat Bay earthquakes. American Geophysical Union: Active Tectonics and Seismic Potential of Alaska, *Geophysical Monograph Series 179*, DOI: https://doi.org/10.1029/179GM21.

Plafker, G., Hudson,T., Bruns, T.R., and Rubin, M. (1978). Late Quaternary offsets along the Fairweather faults and crustal plate interactions in southern Alaska. *Canadian Journal of Earth Sciences,* **15**(5), 805–816, DOI: https://doi.org/10.1139/e78-085.

Rollins, C. *et al.* (2020). In preparation.

Ruppert, N.A. (2008). Stress map for Alaska from earthquake focal mechanisms. American Geophysical Union*:* Active Tectonics and Seismic Potential of Alaska, *Geophysical Monograph Series,* **179**, 351–367, DOI: https://doi.org/10.1029/179GM20.

Sauber, J. M., and Molnia, B.F. (2004). Glacier ice mass fluctuations and fault instability in tectonically active Southern Alaska. *Global and Planetary Change,* **42**, 279–293, DOI: https://doi.org/10.1016/j.gloplacha.2003.11.012.

Sauber, J. M., and Ruppert, N. (2008). Rapid Ice Mass Loss: Does it Have an Influence on Earthquake Occurrence in Southeast Alaska? American Geophysical Union: Active Tectonics and Seismic Potential of Alaska, *Geophysical Monograph Series,* **179**, DOI: https://doi.org/10.1029/179GM21.

Sauber, J., Plafker, G., and Gipson, J. (1995). Geodetic measurements used to estimate ice transfer during Bering Glacier surge. *Eos, Transactions American Geophysical Union,* **76**(29), 289–290, DOI: https://doi.org/10.1029/95EO00171.

Sauber, J., McClusky, S., and King, R. (1997). Relation of ongoing deformation rates to the subduction process in southern Alaska. *Geophysical Research Letters,* **24**, 2853–2856, DOI: https://doi.org/10.1029/97GL52979.

Sauber, J., Plafker, G., Molnia, B.F., and Bryant, M.A. (2000). Crustal deformation associated with glacial fluctuations in the eastern Chugach Mountains, Alaska. *Journal of Geophysical Research,* **105**, 8055–8077, DOI: https://doi.org/10.1029/1999JB900433.

Sauber, J.M., Freymueller, J.T., Han, S.C., Davis, J.L., and Ruppert, N.A. (2016), Short-term response of the solid Earth to cryosphere fluctuations and the earthquake cycle in south-central Alaska.

American Geophysical Union, Fall Meeting 2016, abstract #G11A-1057. (poster available on Researchgate).

Spada, G., *et al*. (2003). TABOO, User Guide. Samizdat Press, Golden-White River Junction.

Steffen, R., Wu, P., and Lund, B. (2021). Geomechanics of glacially-triggered faulting. In H. Steffen, O. Olesen, and R. Sutinen, eds, *Glacially-Triggered Faulting*, pp. **–**.

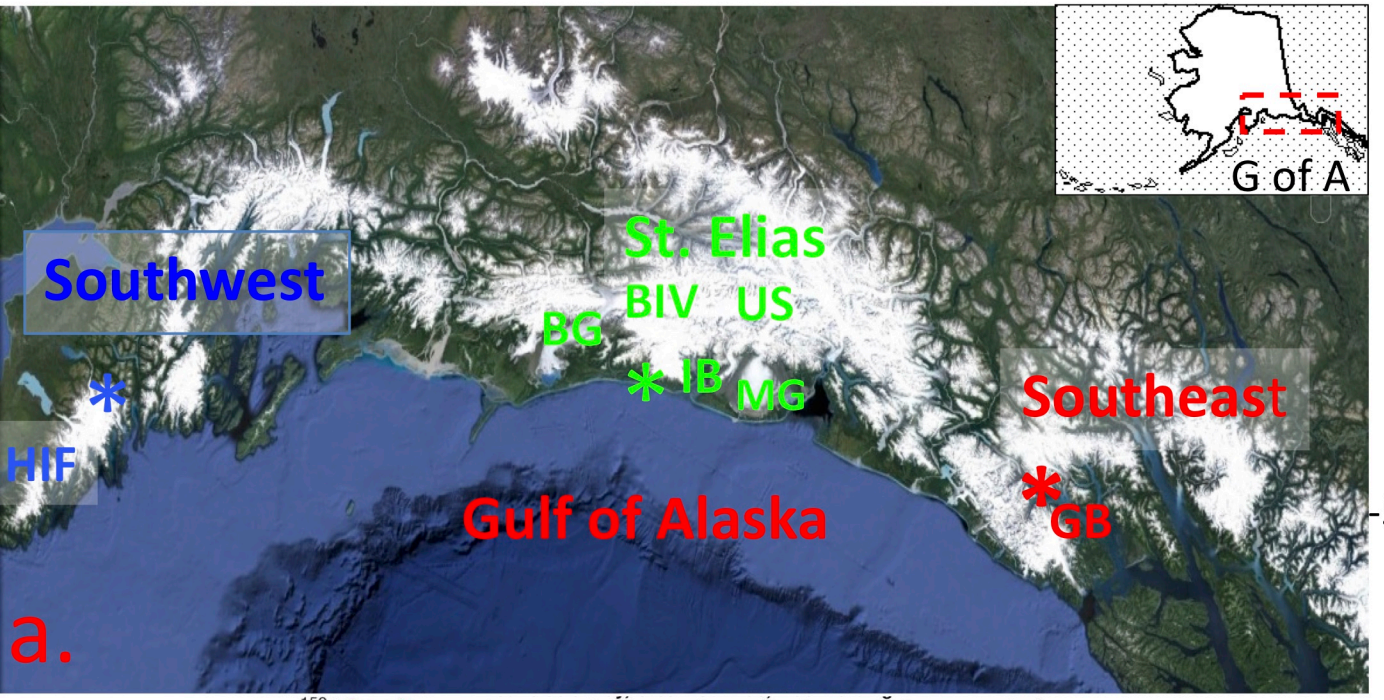
G of A
Southwest
St. Elias
BIV
US
BG
IB
MG
HIF
Gulf of Alaska
Southeast
GB
-59.0
a.

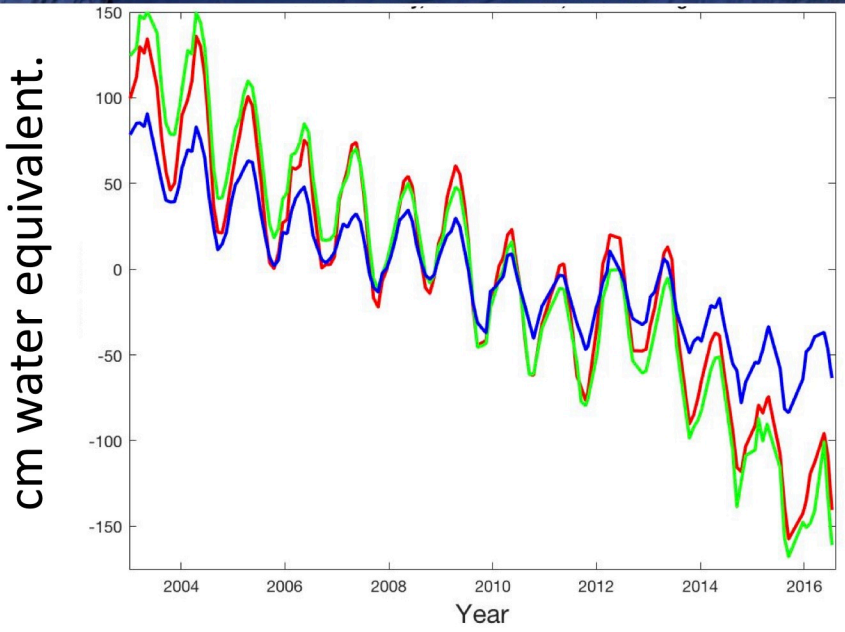
cm water equivalent.
150
100
50
0
-50
-100
-150
2004
2006
2008
2010
2012
2014
2016
Year

b.

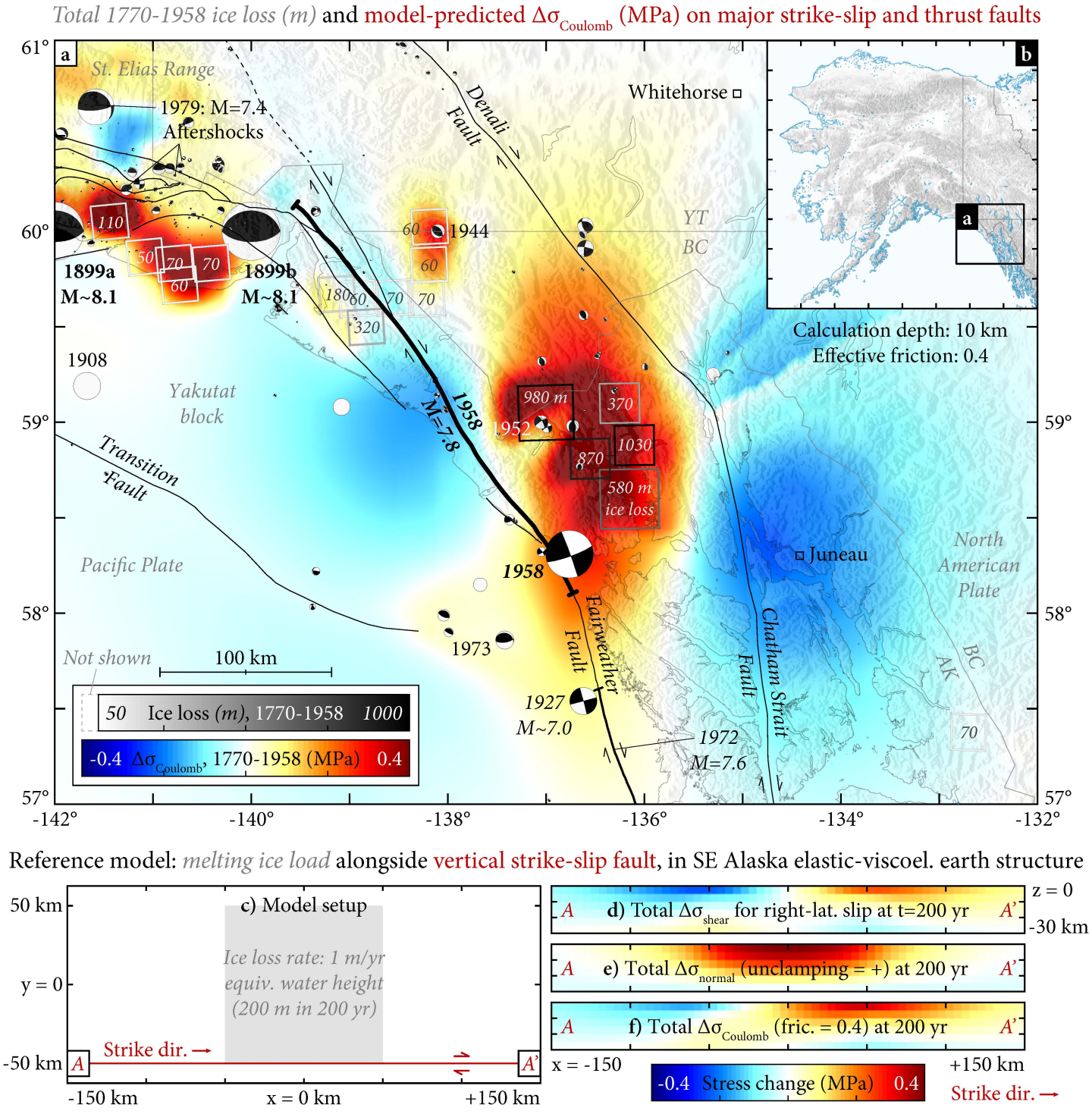

Reference model: *melting ice load* alongside vertical strike-slip fault, in SE Alaska elastic-viscoel. earth structure

Winter:

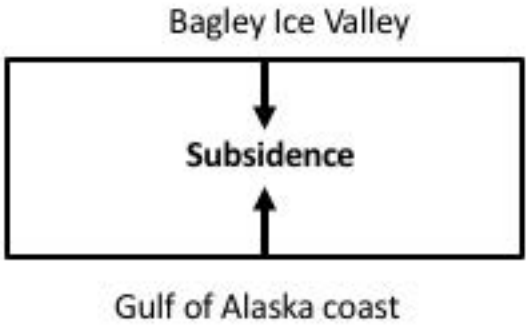

Change in CFS due to Cryospheric <u>Loading</u>:
promotes fault stability

Inland : -21 kPa

Coastal Region: -4 kPa

Summer:

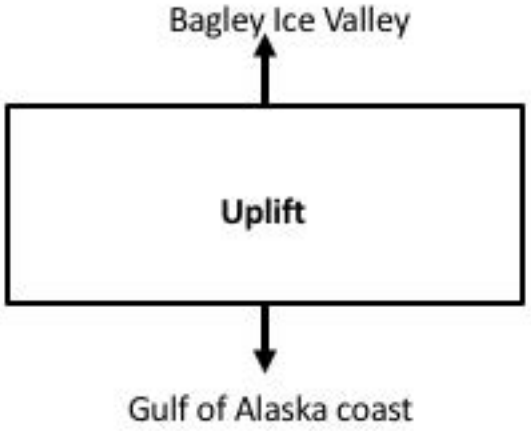

Change in CFS due to Cryospheric <u>Unloading</u>:
promotes fault instability

Inland: 26* kPa

Coastal Region : 5 kPa

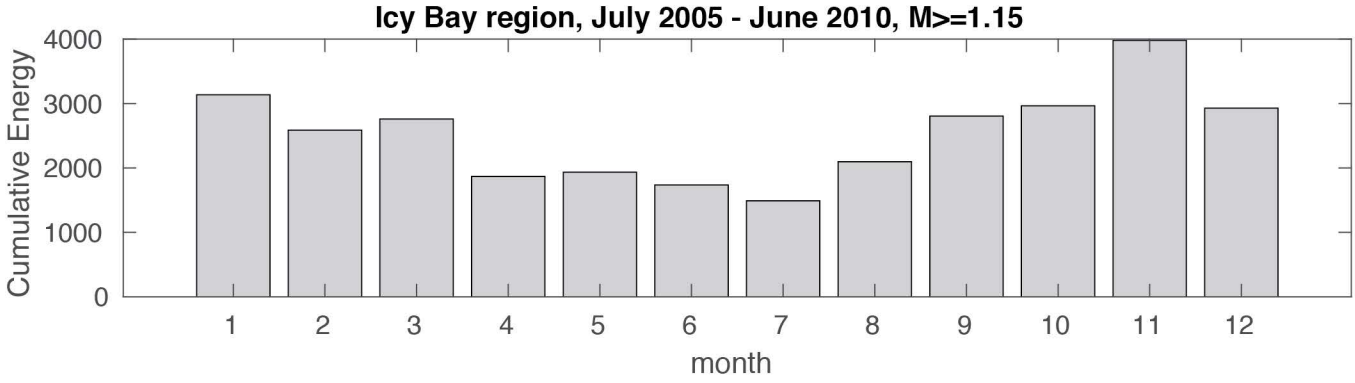
Icy Bay region, July 2005 - June 2010, M>=1.15
Cumulative Energy
0
1000
2000
3000
4000
1
2
3
4
5
6
7
8
9
10
11
12
month

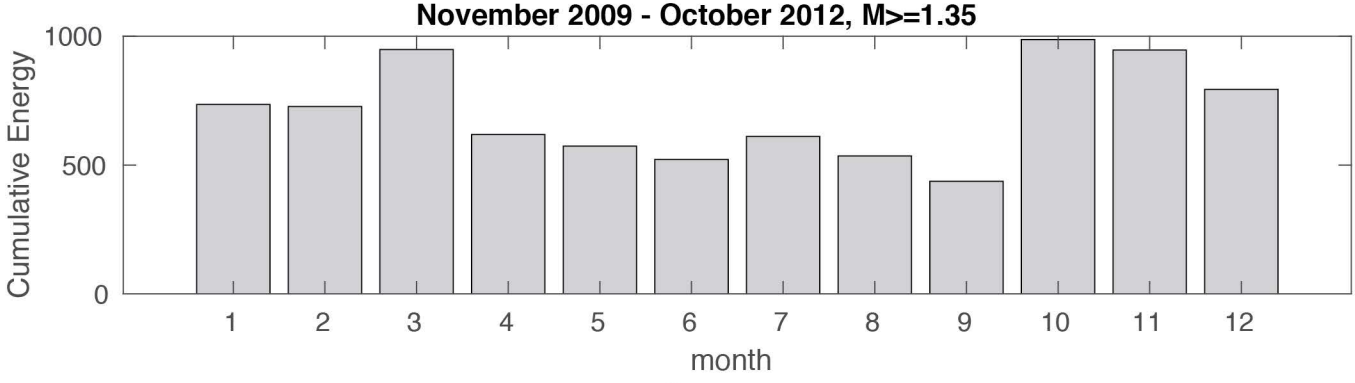
November 2009 - October 2012, M>=1.35
Cumulative Energy
0
500
1000
1
2
3
4
5
6
7
8
9
10
11
12
month

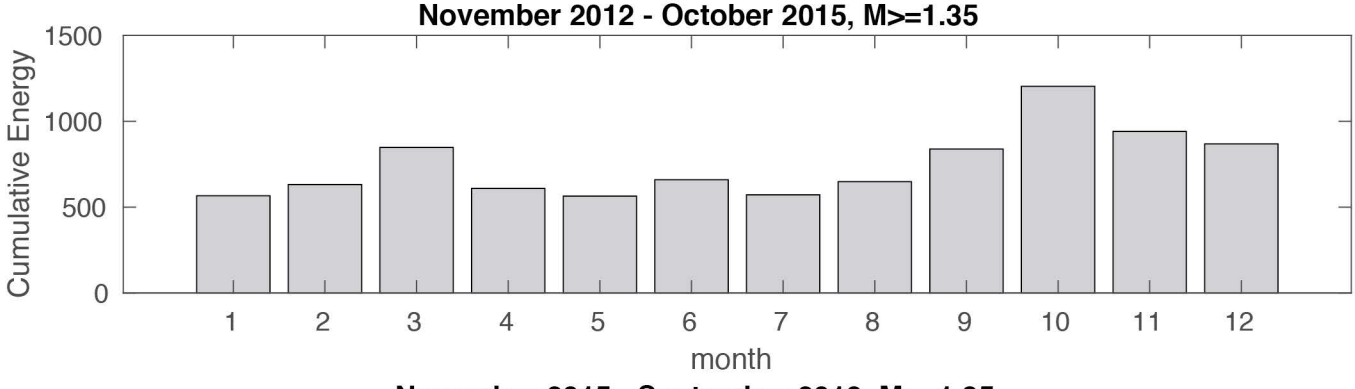
November 2012 - October 2015, M>=1.35
Cumulative Energy
0
500
1000
1500
1
2
3
4
5
6
7
8
9
10
11
12
month

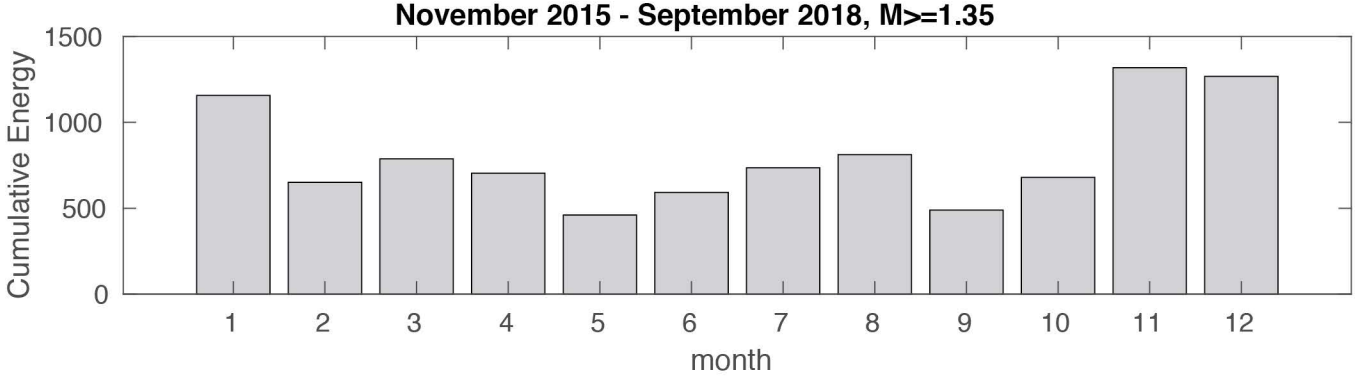
November 2015 - September 2018, M>=1.35
Cumulative Energy
0
500
1000
1500
1
2
3
4
5
6
7
8
9
10
11
12
month

All months (474 events)

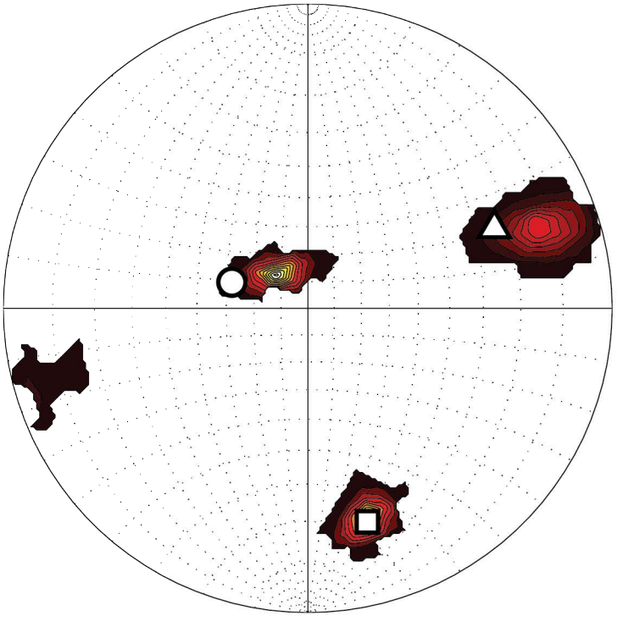

S1
S2
S3

S1: trend: 164.4; plunge: 17.8
S2: trend: 66.8; plunge: 22.6
S3: trend: –70.8; plunge: 60.5
Faulting style: Thrust

Summer months (May-Aug., 188 events)

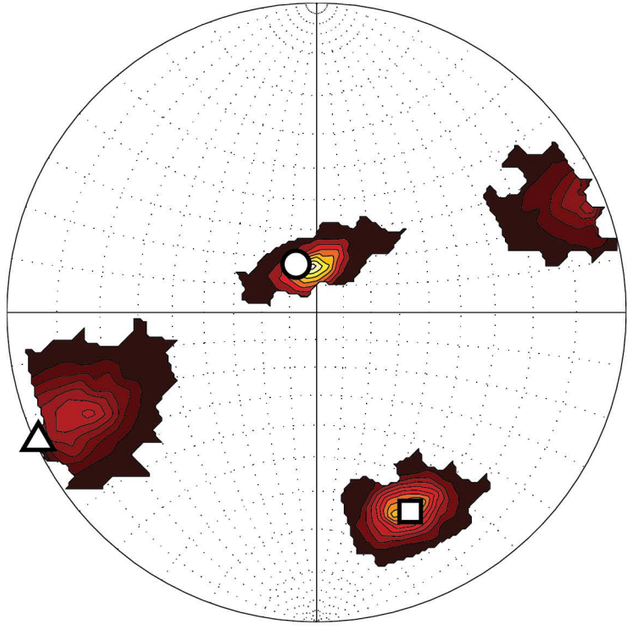

S1
S2
S3

S1: trend: 154.8; plunge: 19.2
S2: trend: –114.8; plunge: 0.6
S3: trend: –23.1; plunge: 70.7
Faulting style: Thrust

Winter months (Nov.-Feb., 140 events)

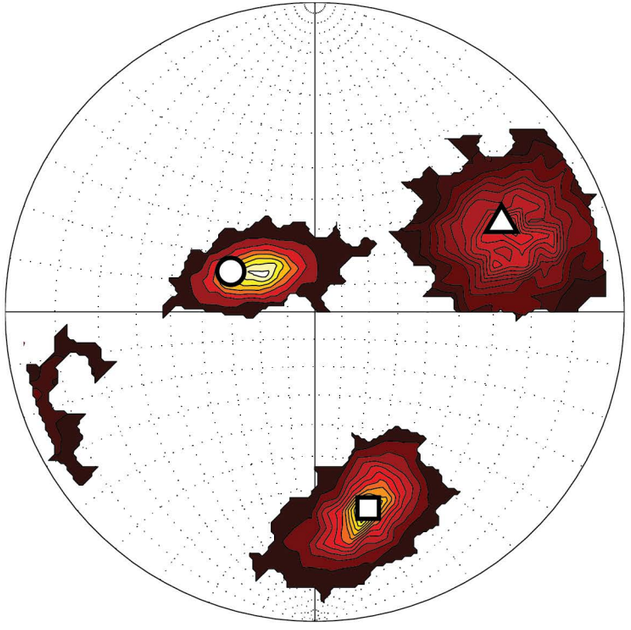

S1
S2
S3

S1: trend: 164.8; plunge: 23.4
S2: trend: 64.5; plunge: 22.5
S3: trend: –64.2; plunge: 56.4
Faulting style: Thrust